Research Article | Vol. 28, No. 12 / 8 June 2020 / Optics Express 18006
Optics EXPRESS

Walk-off controlled self-starting frequency combs in $\chi^{(2)}$ optical microresonators

S. Smirnov,[1] B. Sturman,[2] E. Podivilov,[2] and I. Breunig[3,4,*]

[1] Novosibirsk State University, 630090 Novosibirsk, Russia
[2] Institute of Automation and Electrometry of RAS, 630090 Novosibirsk, Russia
[3] University of Freiburg, Department of Microsystems Engineering - IMTEK, Georges-Köhler-Allee 102, 79110 Freiburg, Germany
[4] Fraunhofer Institute for Physical Measurement Techniques IPM, Heidenhofstr. 8, 79110 Freiburg, Germany
[*] optsys@ipm.fraunhofer.de

Abstract: Investigations of frequency combs in $\chi^{(3)}$ optical microresonators are burgeoning nowadays. Changeover to $\chi^{(2)}$ resonators promises further advances and brings new challenges. Here, the comb generation entails not only coupled first and second harmonics (FHs and SHs) and two dispersion coefficients but also a substantial difference in the group velocities – the temporal walk-off. We predict walk-off controlled highly stable comb generation, which is drastically different from that known in the $\chi^{(3)}$ case. This includes the general notion of antiperiodic states; formation of localized coherent antiperiodic steady states (solitons), where the FH and SH envelopes move with a common velocity without shape changes; characterization of a new vast family of antiperiodic solitons; and the dependence of comb spectra on the pump power and the group velocity difference.

1. Introduction

Frequency combs [1,2] representing consecutive equidistant optical lines are of great value for metrology, spectroscopy, and other applications [3–5]. During the last decade, microresonator comb concept becomes increasingly important. Generation of high-quality frequency combs in $\chi^{(3)}$ microresonators, see [6–13] and references therein, is one of the most spectacular achievements in nonlinear optics in the last decade. These combs correspond to continuous-wave single-frequency pumped coherent structures circulating along the resonator rim with a constant speed. Typically, these structures are dissipative solitons balancing not only dispersion broadening and nonlinearity, but also external pumping and internal losses [10,13]. They can be substantially different from solitons in the conservative systems. The outstanding comb properties stem from high Q-factors and small volumes of the resonator modes.

Transfer of the comb concept to $\chi^{(2)}$ resonators represents a big challenge and offers new opportunities. Here, there are two light envelopes – the first and second harmonics (FH and SH) – instead of one and, therefore, two dispersion coefficients. Also there is a substantial group velocity difference leading to the temporal walk-off between FH and SH. Furthermore, phase matching has to be ensured for the second-order nonlinear processes. Realization of $\chi^{(2)}$ combs promises lowering pump powers, entering new spectral ranges, and new operation regimes. The presence of subcombs in the FH and SH spectral ranges, see Fig. 1, is a new positive feature.

First attempts were undertaken to explore soliton comb regimes in $\chi^{(2)}$ resonators [14–16]. They concern with nonlinear processes running at the spectral point of equal FH and SH group velocities. The found dissipative solitons are similar to the conservative solitons reviewed in [17]. Walk-off controlled soliton solutions at nonzero pump and zero losses were found [18]; their stability is an open issue. Also, numerical results on analysis of comb regimes regardless of solitons are known [19–22]. There are a few experimental demonstrations of combs in $\chi^{(2)}$

#395360 https://doi.org/10.1364/OE.395360
Journal © 2020 Received 17 Apr 2020; revised 22 May 2020; accepted 22 May 2020; published 1 Jun 2020

Optics EXPRESS

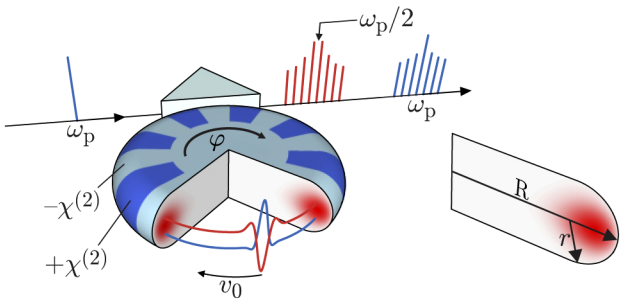

Fig. 1. Schematic of $\chi^{(2)}$ comb generation. Continuous-wave pump at the frequency ω_p generates coupled SH and FH combs in a microresonator owing to cascaded second-order nonlinear processes. These combs correspond to SH and FH solitons moving along the resonator rim with a common velocity v_0. Red spots show localization of the resonator modes; φ is the azimuth angle. Radial poling, i.e. spatial modulation of the sign of $\chi^{(2)}$, and rim shaping via control of the ratio of major (R) and minor (r) radii allow for quasi-phase matching and mode management, respectively.

based resonators, e.g. in bow-tie cavities [20,23,24], in waveguide cavities [25], in whispering gallery resonators [26,27], and in chip-integrated ring resonators [28]. Only in the latter, solitons have been presented.

Still, the overall physical pattern of $\chi^{(2)}$ combs remains obscure.

In this paper, we report on walk-off controlled comb solutions for $\chi^{(2)}$ resonators incorporating pump and losses and applicable to broad ranges of the pump frequency (wavelength). The found solutions belong to a vast general class of antiperiodic states [18], including solitons, which are topologically different from conventional periodic states. Also, they are totally different from periodic solutions of [14–16] and from lossless antiperiodic solutions of [18]. In particular, our comb generation is highly stable, it can start from random noise.

2. Theoretical background

2.1. Basic relations for optical microresonators

High-Q optical microresonators possess a discrete mode spectrum [29–31]. For a resonator with the major radius R, modes can be viewed as quasi-plane waves propagating along the rim and characterized by the azimuth angle φ [29–31], see Fig. 1. The modal functions are 2π-periodic. Following previous comb studies, we restrict ourselves to a single transverse mode type. Each mode is characterized by the azimuth number m or by the wavenumber $k_m = m/R$. For typical $\chi^{(2)}$ resonators, $m \sim 10^4$, and k_m form a quasi-continuous set. The modal frequencies are $\omega_m = 2\pi c/\lambda_m = k_m c/n(\lambda_m)$, where c is the vacuum speed of light, λ_m is the vacuum wavelength, and $n(\lambda)$ is the effective refractive index. The latter is close to the bulk index $n_b(\lambda)$, but includes corrections for the geometric dispersion and vectorial coupling [32–35].

For quadratic nonlinearity, the phase-matching (PM) conditions $\omega_{k_2} = \omega_{k_1} + \omega_{k_1'}$, $k_2 = k_1 + k_1'$ with discrete wavenumbers have to be fulfilled. At $k_1 = k_1'$ they give the SH generation conditions. The latter can be fulfilled for some particular wavelength combinations via employing the birefringence of the material (if there is any) [36]. However, equivalent quasi-PM conditions can by ensured via radial poling, see also Fig. 1 and the Appendix section, practically for any spectral range [37,38]. This admits the presence of small frequency differences, $|\omega_{2k_1} - 2\omega_{k_1}| \ll c/nR$. Fine PM tuning is also available, e.g. via changing the resonator temperature on the mK level, applying the electro-optic effect or changing the geometric size of the resonator using an integrated piezo translator [31,39,40].

Optics EXPRESS

2.2. Envelope equations for periodic and antiperiodic states

Let the (quasi-) PM conditions $\omega_{k_2^0} = 2\omega_{k_1^0}$, $k_2^0 = 2k_1^0$ be fulfilled and the pump frequency ω_p be very close to $\omega_{k_2^0}$ (SH pumping). Here, the azimuth number m_2^0 is even and $m_1^0 = m_2^0/2$ is an integer, see also Fig. 2(a). The light electric field can be represented as

$$S\exp[\mathrm{i}(m_2^0\varphi - \omega_p t)] + F\exp[\mathrm{i}(m_2^0\varphi - \omega_p t)/2] + c.c., \tag{1}$$

where $F(\varphi, t)$ and $S(\varphi, t)$ are complex FH and SH envelopes, both 2π-periodic in φ. These envelopes obey a generic set of nonlinear equations [15,17,18]:

$$\begin{aligned}\left[i\left(\frac{\partial}{\partial t} + \frac{v_1}{R}\frac{\partial}{\partial\varphi} + \gamma_1\right) + \frac{v_1'}{2R^2}\frac{\partial^2}{\partial\varphi^2} - \Delta_1\right]F &= 2\mu SF^*\\ \left[i\left(\frac{\partial}{\partial t} + \frac{v_2}{R}\frac{\partial}{\partial\varphi} + \gamma_2\right) + \frac{v_2'}{2R^2}\frac{\partial^2}{\partial\varphi^2} - \Delta_2\right]S &= \mu F^2 + ih,\end{aligned} \tag{2}$$

where $v_{1,2}$ and $v_{1,2}'$ are the group velocities and the dispersions (discrete equivalents of $d\omega/dk$ and $d^2\omega/dk^2$) at $k_{1,2}^0$, $\gamma_{1,2}$ are the modal decay constants, $\Delta_{1,2}$ are the frequency detunings accounting for a slightly imperfect PM and a small difference $\omega_p - \omega_{k_2^0}$, μ is the coupling constant which is proportional to $\chi^{(2)}$, and h is the pump strength. These parameters are real and experimentally controlled; the ratios $v_{1,2}/2\pi R$ ($\gtrsim$ 10 GHz) are known as the FH and SH free spectral ranges. The polarization types of FH and SH can be the same or different.

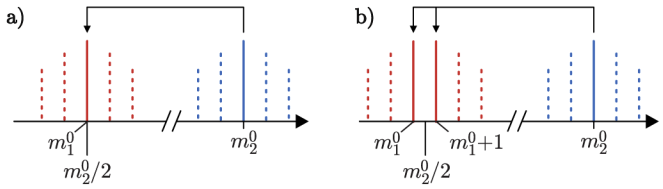

Fig. 2. Excitation of periodic (a) and antiperiodic (b) states for SH-pumping of even and odd modes. The FH carrier frequency $m_2^0/2$ is integer in a) and semi-integer in b). Side harmonics arise automatically in b) above the threshold.

Now let us pump a SH mode with an odd azimuth number m_2^0, see also Fig. 2(b). The PM conditions link this mode to two FH modes possessing even and odd numbers: $\omega_{m_2^0} = \omega_{m_1^0} + \omega_{m_1^0+1}$, $m_2^0 = 2m_1^0 + 1$. The question is whether set (2) is still valid. The answer is *yes*, but the FH envelope becomes antiperiodic, $F(\varphi) = -F(\varphi + 2\pi)$ [18]. This follows from 2π-periodicity of the true light field and the presence of the antiperiodic factor $\exp(\mathrm{i}m_2^0\varphi/2)$ in Eq. (1). The 2π-periodic quantity $|F|^2$ represents the FH field intensity, while the Fourier expansion of $F(\varphi)$ consists of semi-integer harmonics F_{j_1} with $j_1 = m_1 - m_1^0 - 1/2 = \pm 1/2, \pm 3/2, \ldots$. The SH amplitude $S(\varphi)$ remains 2π-periodic; it includes harmonics S_{j_2} with $j_2 = m_2 - m_2^0 = 0, \pm 1, \ldots$. Attempts to employ 2π-periodic FH envelopes break the generic structure of Eqs. (2).

The antiperiodic solutions of Eqs. (2) are topologically different from the periodic ones. They form a separate class of nonlinear states, which is specific for SH pumping and favorable for comb generation. The differences between the periodic and antiperiodic states are crucial:

– In the periodic case, there are spatially uniform solutions $\bar{F}(\varphi), \bar{S}(\varphi) = const$. In the antiperiodic case, such solutions are impossible.

– Harmonics $F_{1/2}$ and $F_{-1/2}$ not only influence S_0, but force harmonics $S_{\pm 1}$ enriching the SH spectrum. The latter cause new nonlinear processes, so that a broad FH spectrum appears above a single oscillation threshold.

Optics EXPRESS

Nonlinear set (2), including many variable parameters, is much more complicated than the well-known Lugiato-Lefever equation [41,42] relevant to $\chi^{(3)}$ comb modeling [10,13]. Here, we restrict ourselves to zero detunings $\Delta_{1,2} = 0$ (exactly fulfilled PM conditions). Also, we set for simplicity $\gamma_{1,2} = \gamma$. Four dimensionless parameters control then the nonlinear behavior. These are the normalized pump strength $\eta = 2\mu h/\gamma^2$, the walk-off parameter $\alpha = v_{12}/\gamma R$ with $v_{12} = v_1 - v_2$, and two dispersion parameters $\beta_{1,2} = v'_{1,2}/2\gamma R^2$. The threshold value of η for generation of the antiperiodic states is $\eta_{\text{th}} = (1 + \beta_1^2/16)^{1/2} \simeq 1$. Thus, parameter η is expressible by the pump power ratio: $\eta^2 = \mathcal{P}/\mathcal{P}_{\text{th}}$, with the oscillation threshold $\mathcal{P}_{\text{th}}$. An estimation of a typical threshold value and its comparison with the one of a $\chi^{(3)}$ based parametric oscillation is found in Appendix B.

Above the threshold, we are eager for antiperiodic steady states $F(\varphi - v_0 t/R)$, $S(\varphi - v_0 t/R)$ moving with a common velocity v_0 without shape changes. Such states provide FH and SH frequency combs; the Fourier components F_{j_1} and S_{j_2} represent the FH and SH frequency comb spectra with the common spacing $\delta\omega = v_0/R$. Periodic steady states with such spacing are not expected for $\Delta_{1,2} = 0$: The background solution $\bar{F}, \bar{S}$ with $|\bar{F}|^2 \propto \eta - \eta_{\text{th}}$ is stable here against spatially uniform and quasi-uniform perturbations. The presence of the antiperiodic states and their stability are not granted. Also, velocity v_0 is unknown, it must be determined simultaneously with the shape of the steady state. Since the parametrically generated satellites $F_{\pm 1/2}$ propagate at the threshold with velocity v_1, one can expect that $v_0 \simeq v_1$ near the threshold. The velocity difference $v_{01} = v_0 - v_1$ is also an important parameter; the ratio $v_{01}/2\pi R$ characterizes fine nonlinear tuning of the frequency comb spacing.

The physical pattern can be clarified taking into account representative dependences $v_{1,2}(\lambda)$ and $v'_{1,2}(\lambda)$ for lithium niobate (LN) crystals, Fig. 3. For mm-sized resonators, the effects of geometric dispersion are weak. The group velocity difference $v_{12} = v_1 - v_2$ ranges from huge values ($\sim 10^8$ cm/s) to zero at $\lambda_2^0 \simeq 1.36\,\mu$m. Setting $R = 1.5$ mm, $\gamma = 10^7$ s^{-1} ($Q \approx 10^8$), we get for the pump wavelength $\lambda_2 \simeq 1\,\mu$m: $\alpha \approx 2 \times 10^2$, $\beta_1 \approx 3 \times 10^{-3}$, and $\beta_2 \approx -3 \times 10^{-2}$. The walk-off effects dominate here over the dispersion ones. When moving to the point of equal group velocities λ_2^0, the coefficient α tends to zero, while β_1 and β_2 remain opposite in sign with $|\beta_{1,2}| \approx 10^{-2}$. Thus, the walk-off effects are controlled by the pump wavelength λ_2; they are relatively small in the close vicinity of λ_2^0.

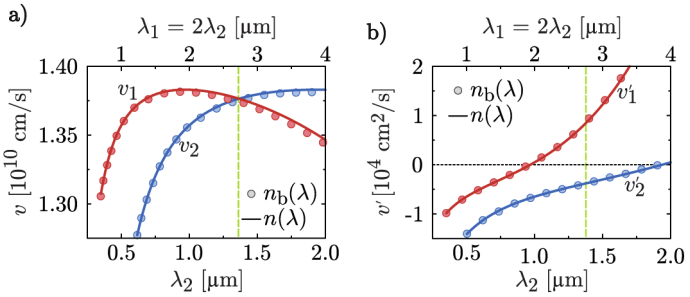

Fig. 3. Wavelength dependences of the group velocities $v_{1,2}$ (a) and the dispersions $v'_{1,2}$ (b) for LN based resonator with $R = 1.5$ mm and $R/r = 3$. The solid and dotted lines refer to the bulk refractive index n_b and the effective index n incorporating the effects of geometric dispersion. The vertical lines $\lambda = \lambda_2^0 = \lambda_1^0/2 \simeq 1.36\,\mu$m correspond to $v_1 = v_2$.

3. Numerical methods and quasi-adiabatic calculation procedure

We simulated numerically the Fourier transform of Eqs. (2) at $\Delta_{1,2} = 0$ in the coordinate frame moving with velocity v_1 using the fourth-order Runge-Kutta method. The total number of Fourier

Optics EXPRESS

harmonics taken into account ranged from 64 to 512. The harmonics $F_{j_1}(t)$ and $S_{j_2}(t)$ were found within a large range of $j_{1,2}$ and within a sufficiently broad range of parameters η, α: $1 \le \eta \le 100$, $10^{-2} \le \alpha \le 10^2$. Accuracy of the calculations was controlled by changing the time step and the total number of harmonics. With the harmonics calculated, one can ensure establishment of the antiperiodic steady states and determine the velocity difference v_{01}, the comb spectra $|F_{j_1}|^2$ and $|S_{j_2}|^2$, and the spatiotemporal profiles $F(\varphi, t)$, $S(\varphi, t)$.

To quantify establishment of the steady state during the temporal evolution, we used the dimensionless discrepancy parameter

$$\varepsilon(t,\tau) = \frac{\sum_j \left|A_j(t) - A_j(t-\tau)\right|^2}{\sum_j \left(|A_j(t)|^2 + |A_j(t-\tau)|^2\right)}, \tag{3}$$

where A_j is one of the harmonics F_{j_1} and S_{j_2} in the coordinate frame moving with an arbitrary velocity v, t is the calculation time, and τ is a variable time shift. As soon as harmonics $A_j(t)$ are known in the frame moving with velocity v_1, they can be recalculated in the frame moving with velocity v through multiplication by $\exp[-ij_{1,2}(v - v_1)t/R]$. Obviously, $\varepsilon(t, \tau)$ turns to zero only when we deal with the steady state and, simultaneously, $v = v_0$. The discrepancy parameter calculated for modestly large evolution times, $\gamma t \gtrsim 10^3$, and minimized over v shows extremely small values ($\varepsilon = 10^{-14} - 10^{-15}$) caused by the numerical noise, see also below. For smaller t, i.e., during the transient stage, it is larger by many orders of magnitude. Thus, we have a numerical tool to control proximity of the steady states and to determine precisely velocity v_0.

The following quasi-adiabatic procedure was used: The pump strength parameter η increased and then decreased stepwise at certain α; the previous values of F_{j_1} and S_{j_2} were used as new initial conditions. At the first step, a weak random noise served as initial condition. Achievement of steady states was controlled with a digital accuracy. The result of temporal evolution was always arrival at a unique coherent FH-SH pattern moving with a common velocity $v_0(\alpha, \eta)$. The sufficient restriction on the pump rise time t_p is $t_p \gtrsim 1\ \mu$s; it is very soft. The found features indicate that the comb generation is self-starting.

Figure 4 shows representative examples of temporal evolution of the FH discrepancy parameter $\varepsilon(t, \tau)$ for the time shift $\tau = 1/\gamma$. The first and second rows correspond to the walk-off parameter $\alpha = 1$ and 0.1. The chosen 17 values η_s are 1.01, 1.1, 1.3, 2., 2.5, 3, 3.5, 4, 5, 7, 10, 12, 15, 18, 20, 25,

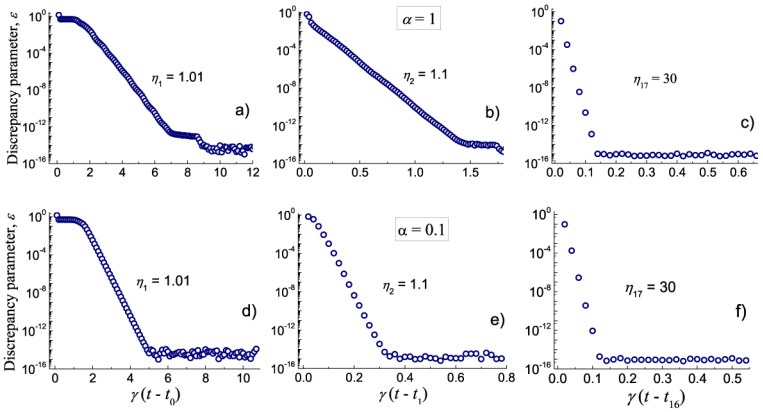

Fig. 4. Six representative evolution runs for the discrepancy parameter $\varepsilon(t, \tau)$ at $\gamma\tau = 1$; the time step is $0.02\gamma^{-1}$. The first and second rows correspond to $\alpha = 1$ and 0.1, respectively. The evolutions relevant to a) and d) start at t_0 from noise and end up at t_1. 512 Fourier harmonics are taken into account, and the model parameters used in the simulations are: $\gamma = 10^7\ \mathrm{s}^{-1}$, $\beta_1 = 0.02$, and $\beta_2 = -0.01$.

Optics EXPRESS

and 30. Subfigures (a), (b), (c) and also (d), (e), (f) exhibit evolution of ε for η_1, η_2, and η_{17}. The most general feature of this evolution is always the same: It is an almost exponential decrease of ε from initial values of the order of 1 to extremely low values $10^{-14} - 10^{-15}$ caused by the numerical noise. Quantitative details of the evolution are also important. The longest evolution, subfigures (a) and (d), starts from modal noise. It takes $\sim (5-7)\gamma^{-1}$ for the harmonics to grow exponentially and reach the saturation. The corresponding evolution time can be identified with the rise time of near-threshold optical parametric oscillation in microresonators. The further evolution runs, which start from regular distributions of the FH and SH harmonics achieved during the previous runs, occur substantially faster. Our choice of 17 steps of evolution to reach the soliton states with $\eta = 30$ is largely arbitrary. In many cases, especially for $\alpha \gtrsim 1$, the same final state can be achieved even in one step. Variation of the time shift τ shows no significant effect on the data of Fig. 4. The temporal evolution of the SH discrepancy parameter behaves in a similar manner.

4. Antiperiodic solitons and comb spectra

Turning to the results, we start with dependences of the comb spectra on α and η. For the FH and SH amplitudes, it is convenient to use the normalized quantities $f = (\mu/\gamma)(2i)^{1/2}F$ and $s = (2\mu/\gamma)S$. With this normalization, the spatially uniform steady states are given by $\bar{f} = \pm(\eta - 1)^{1/2}$ and $\bar{s} = 1$. While all harmonics are nonzero in steady state with antiperiodic boundary conditions, we restrict ourselves to the range $|f_{j_1}|^2, |s_{j_2}|^2 \geq 10^{-4}$ when presenting the comb spectra. The corresponding numbers of significant FH and SH comb lines we denote N_1 and N_2. While this definition is conditional, it is consistent with the litature comb presentations and enables us to quantify the comb strength.

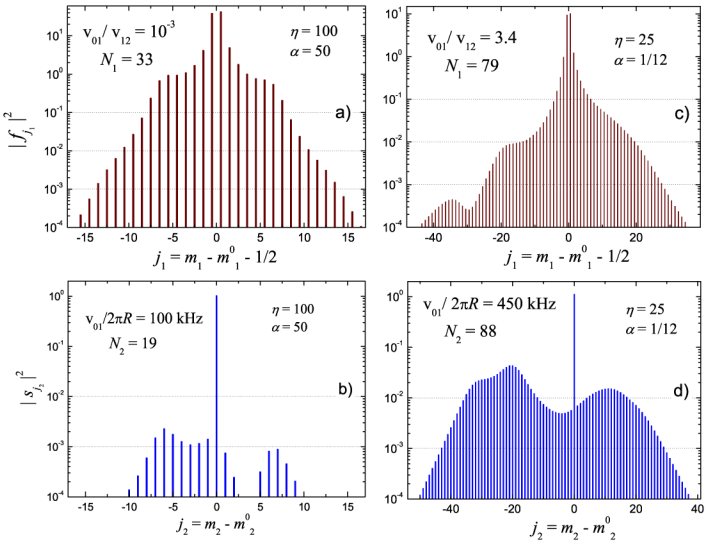

Fig. 5. Steady-state comb spectra $|f_{j_1}|^2$ and $|s_{j_2}|^2$ for two combinations of η and α and the dispersion parameters $\beta_1 = 0.02$ and $\beta_2 = -0.01$. a),b): $\eta = 100$ and $\alpha = 50$; c),d): $\eta = 25$ and $\alpha = 1/12$. Only the comb lines above 10^{-4} are shown. The total number of Fourier harmonics taken into account is 128 for a),b) and 512 for c),d). The frequency spacing between the lines is $\delta\omega = v_0/R$.

Figure 5 shows the normalized comb spectra for two combinations of η and α. For $\alpha = 50$ and $\eta = 100$, representing large α and η, we have $N_1 = 33$, $N_2 = 19$, see Figs. 5(a) and (b), a very small positive velocity ratio $v_{01}/v_{12} \approx 10^{-3}$, and $v_{01}/2\pi R \approx 0.1$ MHz. In the SH spectrum

Optics EXPRESS

there is one dominating line, $|s_0|^2 \simeq 1$. For $\alpha = 1/12$ and $\eta = 25$, representing small walk-off parameters and modest pump strengths, we have well developed FH and SH spectra with $N_1 = 79$ and $N_2 = 88$, see Figs. 5(c) and (d), corresponding to $v_{01}/v_{12} \approx 3.4$ and $v_{01}/2\pi R \approx 0.45$ MHz. Domination of $|s_0|^2$ over the SH wings is less pronounced. The left-right asymmetry of the spectra of Figs. 5(c) and (d) and their ripple structure are caused by an interplay between the walk-off and dispersion effects.

Next, we consider the tuning parameter $v_{01}/2\pi R$ and the total number of comb lines $N_1 + N_2$ as functions of α^{-1}, η within the range $0.1 \le \alpha^{-1} \le 50$, $1 \le \eta \le 30$, see Fig. 6. A remarkable feature is the presence of the vertical line of discontinuity $\alpha = \alpha_c \simeq 1/13$, $\eta > \eta_c \simeq 4.5$. Both mapped quantities grow with increasing η, but this growth is substantially weaker for $\alpha < \alpha_c$. Taken as functions of $\log(1/\alpha)$, they grow first approximately linearly and then drop and stop growing. The drops in a) and b) are relatively large and small. Furthermore, v_{01} tends to zero for $\alpha \to 0$. In essence, the discontinuity marks a sharp transition from the walk-off to dispersion controlled comb regimes for $\eta > \eta_c$. For $\eta < \eta_c$, this transition occurs continuously with increasing $\log(1/\alpha)$. When moving up along the left side of the discontinuity, the tuning parameter approaches the MHz range for $\eta \approx 30$, and the values of v_{01}/v_{12} and $N_1 + N_2 \simeq 2N_1$ approach 3.4 and 180, respectively. Further increase of η presents no difficulties, but can lead to excessively large pump powers. Minor irregularities of map b) at $1/\alpha = 3 - 4$ should not be mixed up with a new discontinuity; they are caused by the mentioned ripple structure of the comb spectra and discreteness of $N_{1,2}$. Remarkably, the discontinuity in Fig. 6(a) looks similar to the discontinuity of SH generation [22] when changing the walk-off parameter.

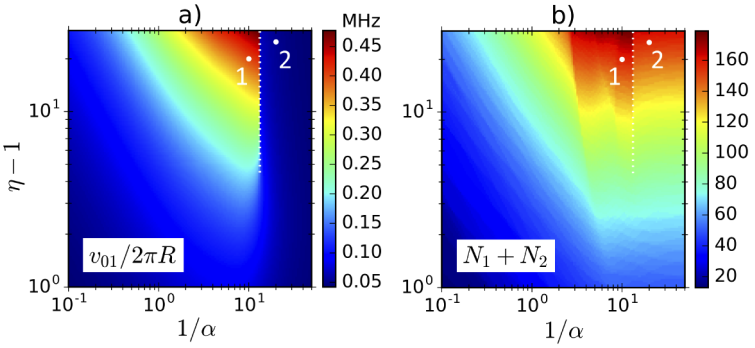

Fig. 6. Maps of the tuning parameter $v_{01}/2\pi R$ (a) and of the total number of significant comb lines $N_1 + N_2$ (b) on the α^{-1}, η plane for $\beta_1 = 0.02$ and $\beta_2 = -0.01$. The vertical line of discontinuity starts at $1/\alpha_c \simeq 13$, $\eta_c \simeq 4.5$. Each map incorporates the data of $151 \times 151 = 22801$ calculation variants with 512 harmonics taken into account. White dots 1 and 2 correspond to the points of the plane $(10, 20)$ and $(20, 25)$ lying to the left and right of the discontinuity and also to profiles **1** and **2** in Fig. 7.

Consider the spatial structure of antiperiodic steady states. Figure 7 shows the FH and SH intensities and phases versus the azimuth angle φ for points **1** and **2** on the α^{-1}, η-plane lying slightly to the left and right of the discontinuity in Fig. 6. As evident from a), c), the intensity changes are strong and well localized, we are dealing thus with FH-SH localized solutions (solitons) propagating with the common velocity v_0 without shape changes. Each intensity distribution has a background; the FH and SH backgrounds are given by $\bar{f}^2 = \eta - 1$ and $\bar{s}^2 = 1$. The intensity profiles **1** are much more oscillatory compared to profiles **2**. The phase $\arg[f(\varphi)]$ exhibits sharp π-steps in both cases ensuring the antiperiodic behavior. The behavior of $\arg[s(\varphi)]$ is not always the same: the phase profiles **1** and **2** in Fig. 7(d) show 2π-drop and 0-change. While the oscillatory behavior of FH and SH intensity may look unusual, it is has similarities among the conservative temporal $\chi^{(2)}$ solitons [17].

Optics EXPRESS

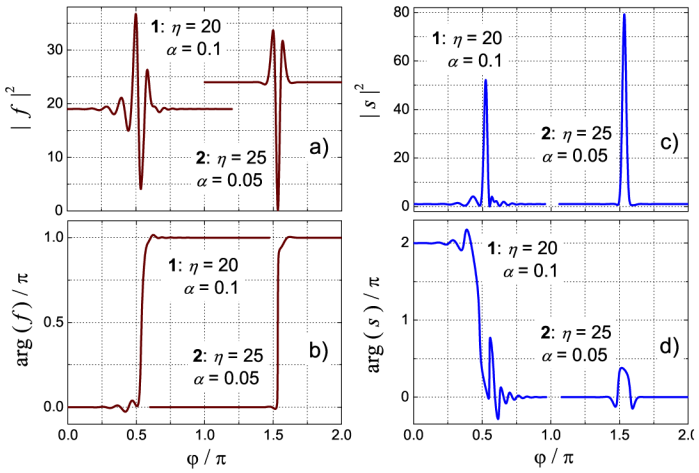

Fig. 7. Antiperiodic solitons for points **1** and **2** lying to the left and right of the discontinuity in Fig. 6. Sub-figures a) to d) show $|f(\varphi)|^2$, arg$[f(\varphi)]$, $|s(\varphi)|^2$, and arg$[s(\varphi)]$. The background values of $|f|^2$ and $|s|^2$ are $\eta - 1$, and 1, respectively. The π-steps of arg$[f(\varphi)]$ in b) occur at the points of minimum of $|f(\varphi)|^2$ in a). Changes of arg$[s(\varphi)]$ occur near the maxima of $|s(\varphi)|^2$, they are qualitatively different for **1** and **2**. 512 FH and SH harmonics are taken into account.

Decrease of α beyond ≈ 0.05 gives no effect, the profiles **2** in Fig. 7 correspond practically to the limit $\alpha \to 0$. Increasing α compared 0.1 causes a weak bifurcation of soliton **1**: the 2π-drop of arg(s) changes to 0. This bifurcation is not accompanied by discontinuities of v_{01} and $N_{1,2}$. Above we focused on the spectral range $\lambda_2 < \lambda_2^0 \simeq 1.36\,\mu$m, where $v_{12}(\lambda_2) > 0$, see Fig. 3. Generalization to the range $\lambda_2 > \lambda_2^0$, where $v_{12} < 0$, presents no difficulties. It results in changing sign of v_{01}. Modest variations of $\beta_{1,2}$ and of the ratio γ_1/γ_2 influence quantitative details, but not the physical pattern.

Our numerical simulations evidence that the coherent antiperiodic soliton states represented by Figs. 5–7 are very robust: Not too abrupt turning the pump power on, with the pump rise time t_p exceeding $10\gamma^{-1}$, ensures achievement of these comb states. This restriction, relevant actually to $t_p \gtrsim 1\,\mu$s, is very soft. For $\eta \gg 1$ and an abrupt (non-adiabatic) turning the pump on, the above scenario of nonlinear evolution to unique steady states can be violated. In this case, generation of single-soliton steady states from noise occurs probabilistically, and complicated multi-soliton structures become visible and most probable. Note lastly that the terms spatial and temporal properties of solitons, as described by functions of $\varphi - v_0 t/R$, are interrelated and interchangeable.

5. Discussion

The results found for $\chi^{(2)}$ resonators concern with new antiperiodic nonlinear comb states that are topologically different from conventional periodic states. To excite the antiperiodic states, it is sufficient to pump SH modes with odd azimuth numbers. Neither $\chi^{(3)}$ nor FH pumped $\chi^{(2)}$ resonators possess such states. The antiperiodic states are the most favorable for $\chi^{(2)}$ comb generation.

The necessary condition for the generation of $\chi^{(2)}$ frequency combs, formation of FH and SH envelopes propagating with a common constant velocity without shape changes, is fulfilled within broad ranges of experimental parameters, the wavelength and power. Moreover, the comb

Optics EXPRESS

states are self-starting – the nonlinear evolution leads above the threshold to a unique comb state under weak limitations on the pump rise time.

In contrast to the theoretical $\chi^{(2)}$ comb studies [14–16], we are not attached to the spectral point of equal FH and SH group velocities λ_2^0. The temporal walk-off of the FH and SH envelopes, caused by generic group velocity difference, controls the spectral features of the comb solutions together with the pump power. In this narrow sense our study is similar to [20–22]. However, in contrast to these studies, we are dealing with the antiperiodic steady states and zero frequency detunings.

Broad comb spectra correspond to a vast family of spatially narrow antiperiodic dissipative solitons. These solitons not only balance the dispersion broadening and nonlinear narrowing, gain and losses, but also ensure a common velocity of FH and SH envelopes. To the best of our knowledge, this multiparametric soliton family has no analogues in the literature.

The case of zero detunings considered, $\Delta_{1,2} = 0$, corresponds to the lowest possible $\chi^{(2)}$ threshold pump powers $\mathcal{P}_{\text{th}}$, so that we are typically far below the $\chi^{(3)}$ threshold powers. For nonzero detunings the influence of the $\chi^{(3)}$ nonlinearity should sometimes be taken into account [16].

6. Conclusions

We have predicted the presence of vast and highly robust family of antiperiodic soliton states relevant to the SH excitation of $\chi^{(2)}$ microresonators. This family corresponds to zero frequency detunings for the first and second harmonics, i.e. to the lowest pump power threshold, and gives broad frequency comb spectra in the FH and SH regions. Importantly, the found family incorporates both the effects of temporal walk-off and frequency dispersion for the FH and SH envelopes. It has a big potential for experimental realization and further extension by incorporating the effects of FH and SH frequency detunings.

Appendix A: effect of radial poling

The nonlinear response of ferroelectric $\chi^{(2)}$ materials, like $LiNbO_3$ or $LiTaO_3$, is determined by the independent real d_{333} and d_{311} components of the third-rank quadratic susceptibility tensor $\hat{d}$ [43,44]. These components change sign under inversion of the direction of the spontaneous polarization. In the case of perfect radial poling, shown schematically in Fig. 1, any of these components (let it be d with the bulk value d_{bulk}) alternates periodically in a stepwise manner with the azimuth angle φ, as illustrated in Fig. 8(a). At the same time, the linear susceptibility tensor and the linear optical properties stay unchanged. If N is the number of alternation periods, the function $d(\varphi)$ is $2\pi/N$-periodic. It can be expanded in the Fourier series

$$d = \sum_j d_j \exp(\mathrm{i}j\varphi) \,, \tag{4}$$

with $j = 0, \pm N, \pm 2N, \ldots$ In the case of $\pm$ symmetric radial domain structure, which is the most suitable for quasi-phase matching, only the Fourier harmonics with odd ratios $j/N = \pm 1, \pm 3, \ldots$ are nonzero [37,45]. For these harmonics we have $|d_j| = 2d_{\text{bulk}}N/\pi|j|$. The reduction factor $|d_j|/d_{\text{bulk}}$ decreases with increasing $|j|/N$, but remains comparable with 1 for $|j| = N$, see also Fig. 8(b).

Employment of the first Fourier harmonics of $d(\varphi)$ for quasi-phase matching corresponds to the SH phase-matching conditions $2\omega_{m_1} = \omega_{2m_1 \pm N}$. The sign "plus" is relevant to the most typical case of decreasing wavelength dependence of the refraction index $n(\lambda)$ [44]. We see that the SH azimuth number $m_2 = 2m_1 \pm N$ is even for even alternation number N and odd for odd number N. In the first case, SH pumping leads to the excitation of periodic states. In the case of odd combination $m_2 \mp N$, the SH quasi-phase matching condition cannot be fulfilled.

Optics EXPRESS

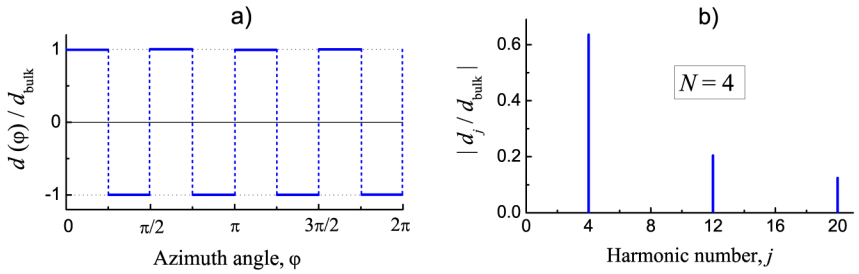

Fig. 8. a) Schematic of the azimuth dependence of the susceptibility coefficient $d(\varphi)$ for a perfect symmetric radial domain pattern with $N = 4$. b) First three harmonics of the corresponding Fourier spectrum with $j = N$, $3N$, and $5N$.

However, we can fulfil the quasi-phase matching condition $\omega_{m_1} + \omega_{m_1+1} = \omega_{2m_1 \pm N}$ leading to the excitation of the antiperiodic states. The values of N typical for the radial poling are of the order of 10^2 [37,38]. Note that the so-called linear poling of $LiNbO_3$ and $LiTaO_3$ crystals [31,46] produces many unnecessary competing Fourier harmonics of $d(\varphi)$; it is not suitable for the comb generation.

Thus, employment of perfect radial poling leads merely to the replacement of the SH azimuth number m_2 by $m_2 \mp N$ and to the replacement of the bulk nonlinear coefficient d_{bulk} by a slightly reduced coefficient $d_{eff} = 2d_{bulk}/\pi$. Generally speaking, one can employ the higher Fourier harmonics for quasi-phase matching. At the same number N, they correspond to substantially different wavelength ranges and also smaller nonlinear coupling coefficients. It is worthy of mentioning that the quasi-phase matching can be combined with continuous fine frequency tuning, such as the temperature tuning or geometric tuning [39,40]. This enables one to accomplish the quasi-phase matching practically in any desirable spectral range.

Appendix B: oscillation thresholds for $\chi^{(2)}$ and $\chi^{(3)}$ based parametric oscillation

The threshold power of a $\chi^{(3)}$ based optical parametric oscillator can be estimated via [47]

$$\mathcal{P}_{th}^{Kerr} \approx 1.54 \frac{\pi}{4} \frac{n^2}{\lambda n_2} V \frac{Q_C}{Q_L} \frac{1}{Q_L^2}, \tag{5}$$

with the refractive index n, the pump wavelength λ, the Kerr coefficient $n_2 \propto \chi^{(3)}$, the effective mode volume V, the coupling and loaded quality factors $Q_{C,L}$. Here, $1/Q_L = 1/Q_C + 1/Q_0$ with the intrinsic quality factor Q_0. Putting $n = 2$, $\lambda = 1550$ nm, $n_2 = 10^{-19}$ m^2/W, $V = 10^{-5} \times 10^{-5} \times 10^{-2}$ m^3, $Q_C = 2 \times 10^7$ and $Q_L = 10^7$, we get $P_{th}^{Kerr} \approx 650$ mW. Now, let us compare this value with the one for a $\chi^{(2)}$ based optical parametric oscillator. Here, we have to take into account that pump light and generated light are in different spectral regions. For the operation close to degeneracy, we have a pump wave at wavelength λ_2 and generated light waves around $\lambda_1 = 2\lambda_2$. Under this assumption, we find for the oscillation threshold [45]

$$\mathcal{P}_{th} \approx \frac{\pi c \varepsilon_0}{16} \frac{n^6}{\lambda_2 d^2} V \frac{Q_{C2}}{Q_{L2}} \frac{1}{Q_{L1}^2 Q_{L2}}, \tag{6}$$

with the vacuum permittivity ε_0, the second-order nonlinear coefficient $d \propto \chi^{(2)}$, the coupling and loaded quality factors $Q_{C2,L2}$ for the pump wave as well as the loaded quality factors Q_{L1} for the generated waves. For simplicity, we have assumed that the refractive index of all interacting waves is n. Taking all resonator related parameters ($n, V, Q_{C2} = Q_C, Q_{L1,2} = Q_L$) from the example above and setting $d = 1$ pm/V, the threshold is approximately 50 μW, i.e. four orders of

Optics EXPRESS

magnitude lower than the one of the third-order based parametric process. That means up to pump powers exceeding 10^4 times the oscillation threshold $\mathcal{P}_{\text{th}}$, we can neglect the influence of third order nonlinearity, i.e. up to $\eta \approx 100$.

Funding

Russian Foundation for Basic Research (20-02-00511); Fraunhofer and Max Planck cooperation programme (COSPA).

Disclosures

The authors declare no conflicts of interest.

References

1. T. Udem, R. Holzwarth, and T. W. Hansch, "Optical frequency metrology," Nature (London) **416**(6877), 233–237 (2002).
2. "Femtosecond Optical Frequency Comb Technology," edited by J. Ye and S. T. Cundiff eds., (Springer, New York, 2005).
3. L. Ma, Z. Bi, A. Bartels, L. Robertsson, M. Zucco, R. Windeler, G. Wilpers, C. Oates, L. Hollberg, and S. A. Diddams, "Optical frequency synthesis and comparison with uncertainty at the 10^{-19} level," Science **303**(5665), 1843–1845 (2004).
4. M. J. Thorpe, K. D. Moll, J. J. Jones, B. Safdi, and J. Ye, "Broadband cavity ringdown spectroscopy for sensitive and rapid molecular detection," Science **311**(5767), 1595–1599 (2006).
5. S. A. Diddams, L. Hollberg, and V. Mbele, "Molecular fingerprinting with the resolved modes of a femtosecond laser frequency comb," Nature (London) **445**(7128), 627–630 (2007).
6. P. Del'Haye, A. Schliesser, O. Arcizet, T. Wilken, R. Holzwarth, and T. J. Kippenberg, "Optical frequency comb generation from a monolitic microresonator," Nature **450**(7173), 1214–1217 (2007).
7. T. Herr, E. Gavartin, M. L. Gorodetsky, R. Holzwarth, and T. J. Kippenberg, "Octave spanning tunable frequency comb from a microresonator," Phys. Rev. Lett. **107**(6), 063901 (2011).
8. T. J. Kippenberg, R. Holzwarth, and S. A. Diddams, "Microresonator based optical frequency combs," Science **332**(6029), 555–559 (2011).
9. T. Herr, K. Hartinger, J. Riemensberger, C. Y. Wang, E. Gavartin, R. Holzwarth, M. L. Gorodetsky, and T. J. Kippenberg, "Universal formation dynamics and noise of Kerr-frequency combs in microresonators," Nat. Photonics **6**(7), 480–487 (2012).
10. T. Herr, V. Brasch, J. D. Jost, C. Y. Wang, N. M. Kondratiev, M. L. Gorodetsky, and T. J. Kippenberg, "Temporal solitons in optical microresonators," Nat. Photonics **8**(2), 145–152 (2014).
11. X. Yi, Q.-F. Yang, K. Y. Yang, M.-G. Suh, and K. Vahala, "Soliton frequency comb at microwave rates in a high-Q silica microresonator," Optica **2**(12), 1078 (2015).
12. M. G. Suh and K. Vahala, "Gigahertz-repetition-rate soliton microcombs," Optica **5**(1), 65 (2018).
13. T. J. Kippenberg, A. L. Gaeta, M. Lipson, and M. L. Gorodetsky, "Dissipative Kerr solitons in optical microresonators," Science **361**(6402), eaan8083 (2018).
14. T. Hannson, P. Parra-Rivas, M. Bernard, F. Leo, L. Gelens, and S. Wabnitz, "Quadratic sioliton combs in doubly resonant second-harmonic generation," Opt. Lett. **43**(24), 6033–6036 (2018).
15. A. Villois and D. Skryabin, "Soliton and quasi-soliton frequency combs due to second harmonic generation in microresonators," Opt. Express **27**(5), 7098 (2019).
16. A. Villois N. Kondratiev, I. Breunig, D. N. Puzyrev, and D. V. Skryabin, "Frequency combs in a microring optical parametric oscillator," Opt. Lett. **44**(18), 4443–4446 (2019).
17. A. V. Buryak, P. Di Trapani, D. V. Skryabin, and S. Trillod, "Optical solitons due to quadratic nonlinearities: from basic physics to futuristic applications," Phys. Rep. **370**(2), 63–235 (2002).
18. E. Podivilov, S. Smirnov, I. Breunig, and B. Sturman, "Nonlinear solutions for $\chi^{(2)}$ frequency combs in optical microresonators," Phys. Rev. A **101**(2), 023815 (2020).
19. F. Leo, T. Hansson, I. Ricciardi, M. De Rosa, S. Coen, S. Wabnitz, and M. Erkintalo, "Walk-off-induced modulation instability, temporal pattern formation, and frequency comb generation in cavity-enhanced second-harmonic generation," Phys. Rev. Lett. **116**(3), 033901 (2016).
20. S. Mosca, I. Ricciardi, M. Parisi, P. Maddaloni, L. Santamaria, P. De Natale, and M. De Rosa, "Direct generation of optical frequency combs in $\chi^{(2)}$ nonlinear cavities," Nanophotonics **5**(2), 316–331 (2016).
21. S. Mosca, M. Parisi, I. Ricciardi, F. Leo, T. Hansson, M. Erkintalo, P. Maddaloni, P. De Natale, S. Wabnitz, and M. De Rosa, "Modulation instability induced frequency comb generation in a continuously pumped optical parametric oscillator," Phys. Rev. Lett. **121**(9), 093903 (2018).
22. F. Leo, T. Hansson, I. Ricciardi, M. De Rosa, S. Coen, S. Wabnitz, and M. Erkintalo, "Frequency-comb formation in doubly resonant second-harmonic generation," Phys. Rev. A **93**(4), 043831 (2016).

Optics EXPRESS

23. V. Ulvila, C. R. Phillips, L. Halonen, and M. Vainio, "Frequency comb generation by a continuous-wave pumped optical parametric oscillator based on cascading quadratic nonlinearities," Opt. Lett. **38**(21), 4281 (2013).
24. I. Ricciardi, S. Mosca, M. Parisi, P. Maddaloni, L. Santamaria, P. De Natale, and M. De Rosa, "Frequency comb generation in quadratic nonlinear media," Phys. Rev. A **91**(6), 063839 (2015).
25. R. Ikuta, M. Asano, R. Tani, T. Yamamoto, and T. N. Imoto, "Frequency comb generation in a quadratic nonlinear waveguide resonator," Opt. Express **26**(12), 15551 (2018).
26. J. Szabados, D. N. Puzyrev, Y. Minet, L. Reis, K. Buse, A. Villois, D. V. Skryabin, and I. Breunig, "Frequency comb generation via cascaded second-order nonlinearities in microresonators," Phys. Rev. Let. **124**, 203902 (2020).
27. I. Hendry, L. S. Trainor, Y. Xu, S. Coen, S. G. Murdoch, H. G. L. Schwefel, and M. Erkintalo, "Experimental observation of internally pumped parametric oscillation and quadratic comb generation in a $\chi^{(2)}$ whispering-gallery-mode microresonator," Opt. Lett. **45**(5), 1204 (2020).
28. A. W. Bruch, X. Liu, Z. Gong, J. B. Surya, M. Li, C. L. Zou, and H. X. Tang, "Pockels Soliton Microcomb," arXiv:2004.07708 (2019).
29. K. J. Vahala, "Optical microcavities," Nature **424**(6950), 839–846 (2003).
30. V. S. Ilchenko and A. B. Matsko, "Optical resonators with whispering-gallery modes, Part I: Basics," IEEE J. Quantum Electron. **12**(1), 15–32 (2006).
31. D. Strekalov, Ch. Marquardt, A. Matsko, H. Schwefel, and G. Leuchs, "Nonlinear and quantum optics with whispering gallery resonators," J. Opt. **18**(12), 123002 (2016).
32. M. Gorodetsky and A. Fomin, "Geometrical theory of whispering-gallery modes," IEEE J. Sel. Top. Quantum Electron. **12**(1), 33–39 (2006).
33. M. L. Gorodetsky and Y. A. Demchenko, "Accurate analytical estimates of eigenfrequencies and dispersion in whipering-gallery spheroidal resonators," Proc. SPIE **8236**, 823623 (2012).
34. I. Breunig, B. Sturman, F. Sedlmeir, H. G. L. Schwefel, and K. Buse, "Whispering gallery modes at the rim of an axisymmetric optical resonator: Analytical versus numerical description and comparison with experiment," Opt. Express **21**(25), 30683 (2013).
35. B. Sturman, E. Podivilov, C. S. Werner, and I. Breunig, "Vectorial perturbation theory for axisymmetric whispering gallery resonators," Phys. Rev. A **99**(1), 013810 (2019).
36. J. U. Fürst, D. V. Strekalov, D. Elser, M. Lassen, U. L. Andersen, C. Marquardt, and G. Leuchs, "Naturally phase-matched second-harmonic generation in a whispering-gallery-mode resonator," Phys. Rev. Lett. **104**(15), 153901 (2010).
37. T. Beckmann, H. Linnenbank, H. Steigerwald, B. Sturman, D. Haertle, K. Buse, and I. Breunig, "Highly tunable low-threshold optical parametric oscillation in radially poled whispering gallery resonators," Phys. Rev. Lett. **106**(14), 143903 (2011).
38. M. Mohageg, D. V. Strekalov, A. A. Savchenkov, A. B. Matsko, V. S. Ilchenko, and L. Maleki, "Calligraphic poling of lithium niobate," Opt. Express **13**(9), 3408 (2005).
39. Ch. Werner, W. Yoshiki, S. Herr, I. Breunig, and K. Buse, "Geometric tuning: spectroscopy using whispering-gallery resonator frequency-synthesizers," Optica **4**(10), 1205–1208 (2017).
40. S. Meisenheimer, J. Fürst, K. Buse, and I. Breunig, "Continuous-wave optical parametric oscillation tunable up to an 8 μm wavelength," Optica **4**(2), 189 (2017).
41. L. A. Lugiato and R. Lefever, "Spatial dissipative structures in passive optical systems," Phys. Rev. Lett. **58**(21), 2209–2211 (1987).
42. I. V. Barashenkov and Y. S. Smirnov, "Existence and stability chart for the ac-driven, damped nonlinear Schrödinger solitons," Phys. Rev. E **54**(5), 5707–5725 (1996).
43. R. W. Boyd, *Nonlinear Optics*, (Academic, 2008).
44. D. N. Nikogosyan, *Nonlinear Optical Crystals: A Complete Survey*, (Springer, 2005).
45. I. Breunig, "Three-wave mixing in whispering gallery resonators," Laser Photonics Rev. **10**(4), 569–587 (2016).
46. V. S. Ilchenko, A. A. Savchenkov, A. B. Matsko, and L. Maleki, "Nonlinear optics and crystalline whispering gallery mode cavities," Phys. Rev. Lett. **92**(4), 043903 (2004).
47. X. Ji, F. A. S. Barbosa, S. P. Roberts, A. Dutt, J. Cardenas, Y. Okawachi, A. Bryant, A. L. Gaeta, and M. Lipson, "Ultra-low-loss on-chip resonators with sub-milliwatt parametric oscillation threshold," Optica **4**(6), 619 (2017).